CrystEngComm

ROYAL SOCIETY OF CHEMISTRY

PAPER

View Article Online
View Journal | View Issue

Cite this: *CrystEngComm*, 2020, **22**, 3943

Tailoring the preferable orientation relationship and shape of α-$FeSi_2$ nanocrystals on Si(001): the impact of gold and the Si/Fe flux ratio, and the origin of α/Si boundaries†

Ivan A. Tarasov, *[a] Tatiana E. Smolyarova,[ab] Ivan V. Nemtsev,[ac] Ivan A. Yakovlev,[a] Mikhail N. Volochaev,[ad] Leonid A. Solovyov,[e] Sergey N. Varnakov[a] and Sergey G. Ovchinnikov[ab]

The growth of α-$FeSi_2$ nanocrystal ensembles on gold-activated and gold-free Si(001) surfaces at different Si/Fe flux ratios *via* molecular beam epitaxy is reported. The study reveals that the utilisation of gold as a catalyst regulates the preferable orientation relationship (OR) of the nanocrystals to silicon and their morphology at a given Si/Fe flux ratio. α-$FeSi_2$ free-standing crystals with continuously tuned sizes from 30 nm up to several micrometres can be grown with an α(001)//Si(001) basic OR under gold-assisted conditions and an α(111)//Si(001) OR under gold-free growth conditions on a Si(001) surface. The preferred morphology of nanocrystals with a particular OR can be altered through changes to the Si/Fe flux ratio. Herein, the microstructure and basic OR between the silicide nanocrystals and the silicon substrate, and the formation of nanocrystal facets were analysed in detail with the help of microscopic techniques and simulation methods based on the analysis of near coincidence site (NCS) distributions at silicide/silicon interfaces. On the basis of the simulations used, we managed to reveal the nature of the interfaces observed for the main types of α-$FeSi_2$ nanocrystals grown. Three types of interfaces typical for nanoplates with an α(001)//Si(001) basic OR, which are (i) stepped, (ii) stressed, and (iii) flat, are explained based on the tendency for the NCS density to increase at the interface. The results presented reveal the potential for the bottom-up fabrication of α-$FeSi_2$ nanocrystals with tuned physical properties as potentially important contact materials and as building blocks for future nanoelectronic devices.

Received 15th March 2020,
Accepted 8th May 2020

DOI: 10.1039/d0ce00399a

rsc.li/crystengcomm

Introduction

Iron and silicon are at the top of the list of abundant chemical elements in the Earth's crust. Deeper insight into iron–silicon compounds, to allow their properties to be adjusted for use in next-generation electronic devices, is required. Widely used in photonics and electronics, InGaAs-based semiconductors have gained popularity due to their unique versatility.[1] These compounds are easily adjustable for band engineering and are not sensitive to intrinsic defects. Among the available Fe–Si compounds, there is only one semiconducting β-$FeSi_2$ phase,[2] which is characterised by its competition for direct and indirect transitions with an energy of around 0.8 eV (ref. 3–5) and its sensitivity to intrinsic defects. It can be utilised as an active material in photon crystals,[6] and also in photovoltaics,[7] thermoelectrics[8,9] and electric charge storage.[10] Finally, the β-$FeSi_2$ phase can be used as an active material in light emission diodes for transmitting signals through optical fibres.[11,12] Overcoming issues related to enhancing its luminescence has been the aim of many research groups.[13–15] Reducing the dimensions of β-$FeSi_2$ down to nanodots, embedded in a silicon matrix or grown on silicon surfaces, with diameters of about 5–20 nm has already shown great potential for enhancing IR photoluminescence and electroluminescence in comparison with β-$FeSi_2$ thin films.[15] β-$FeSi_2$ nanodots with different orientation relationships (ORs) to silicon may be strained in various ways so as to provide a defect-free interface,[2,16,17]

[a] *Kirensky Institute of Physics, Federal Research Center, KSC SB RAS, Krasnoyarsk, 660036, Russia. E-mail: tia@iph.krasn.ru*
[b] *Siberian Federal University, 660041, Krasnoyarsk, Russia*
[c] *Federal Research Center KSC SB RAS, Krasnoyarsk, 660036, Russia*
[d] *Reshetnev Siberian State University of Science and Technology, Krasnoyarsk, 660037, Russia*
[e] *Institute of Chemistry and Chemical Technology, Federal Research Center KSC SB RAS, 660036 Krasnoyarsk, Russia*

† Electronic supplementary information (ESI) available: Additional SEM and TEM measurement data, near coincidence site density maps, schematic representations of the shapes of the nanocrystals, and figures and tables intended to give further details about the origin of α//Si heteroepitaxial interfaces and the role of gold in nanocrystal formation. See DOI: 10.1039/d0ce00399a

which promotes a low concentration of non-radiative recombination centres. However, laser diodes based on β-$FeSi_2$ are still unavailable in the market for wide consumption. Thus, new approaches for the development of competitive technology are also critical.

We propose that the utilisation of other silicon-rich silicides (α-$FeSi_2$, γ-$FeSi_2$, *etc.*) as a buffer layer on silicon ($Fd\bar{3}m$ face-centred diamond-cubic structure; a = 5.43 Å) for the growth of β-$FeSi_2$ nanocrystals may be a useful tool for the strain engineering of the β-$FeSi_2$ phase (which has a base-centred orthorhombic structure with a *Cmca* space group; a = 9.88 Å, b = 7.79 Å, and c = 7.83 Å (ref. 18)), since its bandgap is sensitive to lattice stress.[4,19] One can achieve different strain conditions by varying the OR between β-$FeSi_2$ and α-$FeSi_2$ ($P4/mmm$; a = b = 2.684 Å, c = 5.128 Å (ref. 20)) or γ-$FeSi_2$ ($Fm\bar{3}m$ CaF_2-type structure; a = 5.39 Å (ref. 21)). According to our calculations based on the analysis of NCSs on interfaces, the most relaxed β-$FeSi_2$ phase could grow on α(001) due to this having the closest interatomic and interplanar distances and a high density of NCSs.[22] γ-$FeSi_2$ is not considered at the moment due to its insufficient thermodynamic stability.[23]

In turn, an epitaxially grown α-$FeSi_2$ compound is an object of interest itself. Metallic α-$FeSi_2$ has reportedly been applied as an electrode material with silicon or β-$FeSi_2$ with good ohmic characteristics.[24,25] This phase could also be used for the formation of Schottky barrier contacts,[26] gate electrodes, local interconnects, and diffusion barriers.[27] Nowadays, metal silicides, which have been utilised as contact materials for many decades, face more stringent requirements in terms of contact and series resistance, thermal stability, leakage current induced by rough interface and defects, and silicide thickness control before being utilised in nano metal-oxide-semiconductor field-effect transistors. Thus, further studies are needed to obtain a basic understanding of their formation on silicon substrates.[26,28] Moreover, this paramagnetic and metastable phase under bulk conditions[29] appears to show ferromagnetic properties on the nanoscale, with magnetisation higher than pure iron.[30] Finally, S. Sakane *et al.* recently demonstrated that α-$FeSi_2$ nanodots embedded into epitaxial silicon films promote thermoelectric performance.[9]

Hence, α-$FeSi_2$ appears to be a material with interesting properties that can be tuned *via* specific chemical ordering or stress into α-$FeSi_2$ nanostructures.[31,32] It was reported that endotaxial α-$FeSi_2$ nanowires can be grown by depositing Fe on Si(110) at 650 °C,[33] whereas under similar conditions (600 and 700 °C) the growth of s-$FeSi_2$ and γ-$FeSi_2$ phases occurs, respectively.[21,34] Moreover, these $FeSi_2$ phases and Fe-rich alloy phases with DO3, B2, and A2 crystal structures[35] can coexist under different growth conditions.[36,37] Therefore, this may result in ambiguous phase identification and the contradictory results reported in the available literature. Thus, here we concentrate on examining OR-controllable tetragonal α-$FeSi_2$ phase growth on a Si(001) silicon surface *via* molecular beam epitaxy. The microstructure, basic and interface ORs, and role of gold are considered along with changes in the Fe/Si flux ratio.

Methods

Preparation of α-$FeSi_2$ nanocrystals

α-$FeSi_2$ nanocrystals were formed on a 1°-miscut vicinal p-Si(100) substrate (ρ ~ 5–10 Ω cm) at 840 °C *via* molecular beam epitaxy (MBE) under ultrahigh vacuum (UHV) conditions. Prior to growth, the Si substrate was chemically cleaned *via* the technique described.[38] The Si substrate was exposed to gradual thermal treatment for 3 hours rising to 650 °C at a rate of 4 °C min^{-1} under UHV (base pressure: 6.5 × 10^{-8} Pa). To obtain an atomically clean silicon surface, the wafer was flashed at 850–900 °C until well-ordered (2 × 1) reconstruction appeared in the reflection high-energy electron diffraction pattern. After the specimen was cooled down to room temperature, a gold layer (1 nm) was evaporated from a Knudsen effusion cell onto the substrate surface at a rate of 0.25 nm min^{-1}. Then, the substrate temperature was increased to 840 °C and Fe and Si were deposited simultaneously at rates of 0.1 and 0.34 nm min^{-1} (v_{Si}/v_{Fe} = 3.4) for sample AS1, and 0.23 and 0.13 nm min^{-1} (v_{Si}/v_{Fe} = 0.57) for sample AS2 over 60 min. To highlight the influence of the gold island layer on the growth of $FeSi_2$ nanostructures, the samples S1 and S2 were prepared under the same technological procedure but without gold layer deposition. Additional discussion on the synthesis procedure is given in the ESI.†

Material characterisation

Ex situ determination of the morphologies and phase compositions of the samples was performed *via* scanning electron microscopy (SEM) using Hitachi S-5500 and Hitachi TM3000 microscopes, and *via* transmission electron microscopy using a Hitachi HT7700 microscope equipped with an ED spectrometer (6T/60 Bruker). X-ray diffraction (XRD) analysis was carried out with the help of a PANalytical X'Pert PRO diffractometer equipped with a PIXcel solid-state detector using Cu Kα radiation.

Simulation method

To examine the origin of the faceting of embedded α-$FeSi_2$ nanocrystals into the silicon substrate we used a crystallogeometrical approach, which focuses on the calculation of NCS density. This estimation, with geometrical criteria, despite its simplicity, has already proved its efficiency.[39–41] When two atomic planes with the same symmetry and lattice parameter are superimposed with some rotation and translation, a type of superstructure, a coincidence site lattice, develops. However, in the general case, the coincidence site lattice may not exist and only an NCS lattice can be built. The density of such NCSs with respect to the original lattice is proposed to allow the estimation of the possibility of the epitaxial growth of phases

with such an interface.[42] In this work, the criterion of proximity for NCSs was chosen as 10.8% (~0.59 Å) of the silicon lattice parameter at room temperature (if it is not additionally discussed in the text). The interface area used for calculations was 120 × 120 Å or 400 × 400 Å, and this is additionally noted in the article when necessary. The thickness of the test layer utilised was 0.2 Å. The NCS density is the ratio between a quantity of NCSs in a habit plane and the numbers of atoms in a silicon or α-$FeSi_2$ compound. For calculations, we used the free and open-source software "Phase Transformation Crystallography Lab (PTCLab)".[43] The angle interval used for the calculation of NCS density maps and profiles was 0.5° or 0.1°, which is additionally denoted in the text.

Results and discussion

Morphology and crystal structure characterisation

SEM images of the samples obtained are presented in Fig. 1. One can see that all samples have distinctive features in their morphologies. The nanocrystals appear to be well-shaped, consisting of flat facets with sharp angles, and well-separated, which is typical for samples AS1, S1, and AS2. However, most of the nanocrystals in sample S2 have coalesced (Fig. 1f and h) and have a tendency to form continuous films, losing their geometrical form and clear faceting. Moreover, the average size and density differ. The nanocrystals obtained on gold-activated surfaces (AS1 and AS2) are bigger and sparser on the surface than the ones obtained on the gold-free silicon surfaces. These nanocrystals are more compact and smaller.

It is widely known that gold islands play an important role in determining the growth kinetics for capturing new incoming atoms from the surrounding area and serve as growth centres.[44] Moreover, other peculiarities resulting from an Fe-rich influx (AS2) are observed. The nanocrystals are buried into the silicon substrate (Fig. 1b and d). Additionally, there are voids between the silicide facets and silicon substrates. The depth of such voids can be more than 100 nm (Fig. 1d). The reason for this is that silicon atoms from the substrate tend to be used to accomplish stoichiometry in the growing $FeSi_2$ silicide due to high diffusion at the synthesis temperature (T = 840 °C). The gold creates such conditions so that voids are formed, which is confirmed by the absence of voids on the sample S2 obtained on the gold-free silicon surface.

It is worth highlighting the easily distinguished forms of nanocrystals present in the samples AS1, AS2, and S1 (information about the structural properties of the α-$FeSi_2$ nanocrystals is given in Fig. 2; some nanocrystals discussed below are easily distinguished in Fig. 1, others are better observable in Fig. 3 and in Fig. S1, ESI†).

- The first type is rectangular nanoplates, lying towards the <010> and <011> directions (red rectangles in Fig. 1a and b), with a length, width, and thickness of about 400–800 nm, 300–400 nm, and 30–70 nm, respectively. The nanoplate sizes in AS2 turn out to be a bit larger due to the larger resultant value of atoms deposited in the cases of AS2 and S2. It is seen that the rectangular nanoplates present on the samples AS1 and AS2 are absent on S1 and S2. Hence, one can conclude that gold on the silicon surface at the same Si/Fe flux ratio gives rise to the formation of a distinctive α-$FeSi_2$ silicide nanocrystal form – a rectangular nanoplate.
- The second one is triangular nanoplates (Fig. 1a; green triangles) with lateral sizes varying from 50 nm up to 250 nm. It is interesting to note that the sides of the triangular nanoplates do not run parallel to the low index direction of the Si(001) surface in the sample AS1. One of the triangular nanoplate sides deviates by ~14 degrees from the Si<011> direction (Fig. 3e). In the sample AS2, such nanocrystals point out the Si<011> direction. The crucial role here may be played by the number of silicon atoms evaporated onto the substrate surface, as well as the presence of gold (note, triangular nanoplates are absent on the S1 surface). As can be seen in Fig. 1a the growth conditions with excess silicon (AS1 sample) result in the formation of two

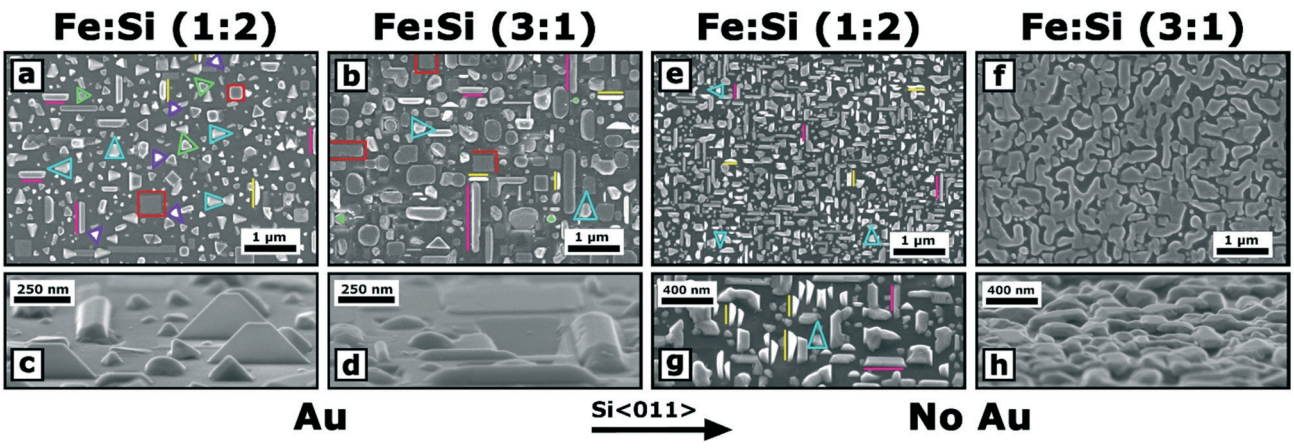

Fig. 1 SEM images of α-$FeSi_2$ nanocrystals: large scale views of the AS1 (a) and AS2 (b) samples, and magnified and tilted views of the AS1 (c) and AS2 (d) samples; and large scale views of the S1 (e) and S2 (f) samples, and magnified and tilted views (g and h), respectively.

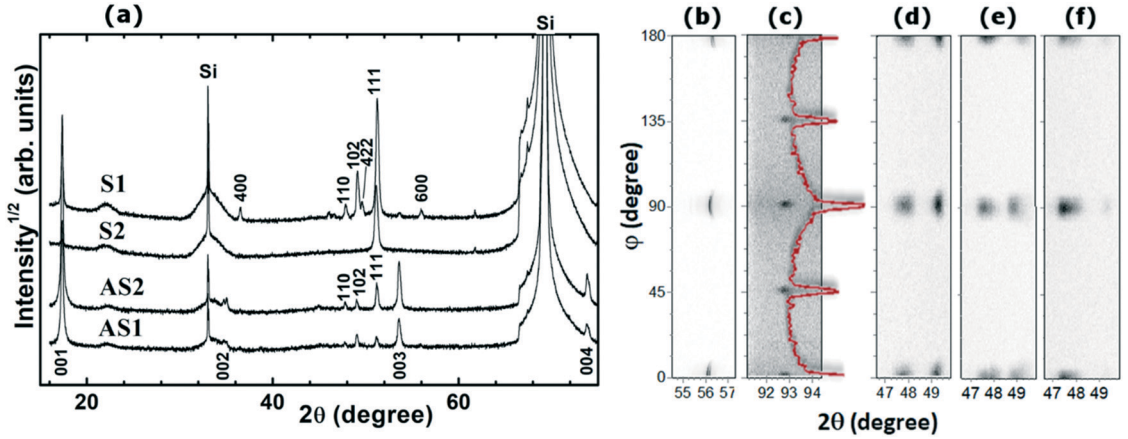

Fig. 2 XRD patterns of the samples AS1, AS2, S2, and S1 (a). Reflection indexes are marked. Images of φ-scans of sample AS2 showing {113} reflections from the Si(100) substrate (b), {114} reflections from α-$FeSi_2$(001)||Si(100) (c), and {110} reflections from α-$FeSi_2$(111)||Si(100) (d). Similar {110} φ-scans for samples S2 and S1 are shown in (e) and (f), respectively.

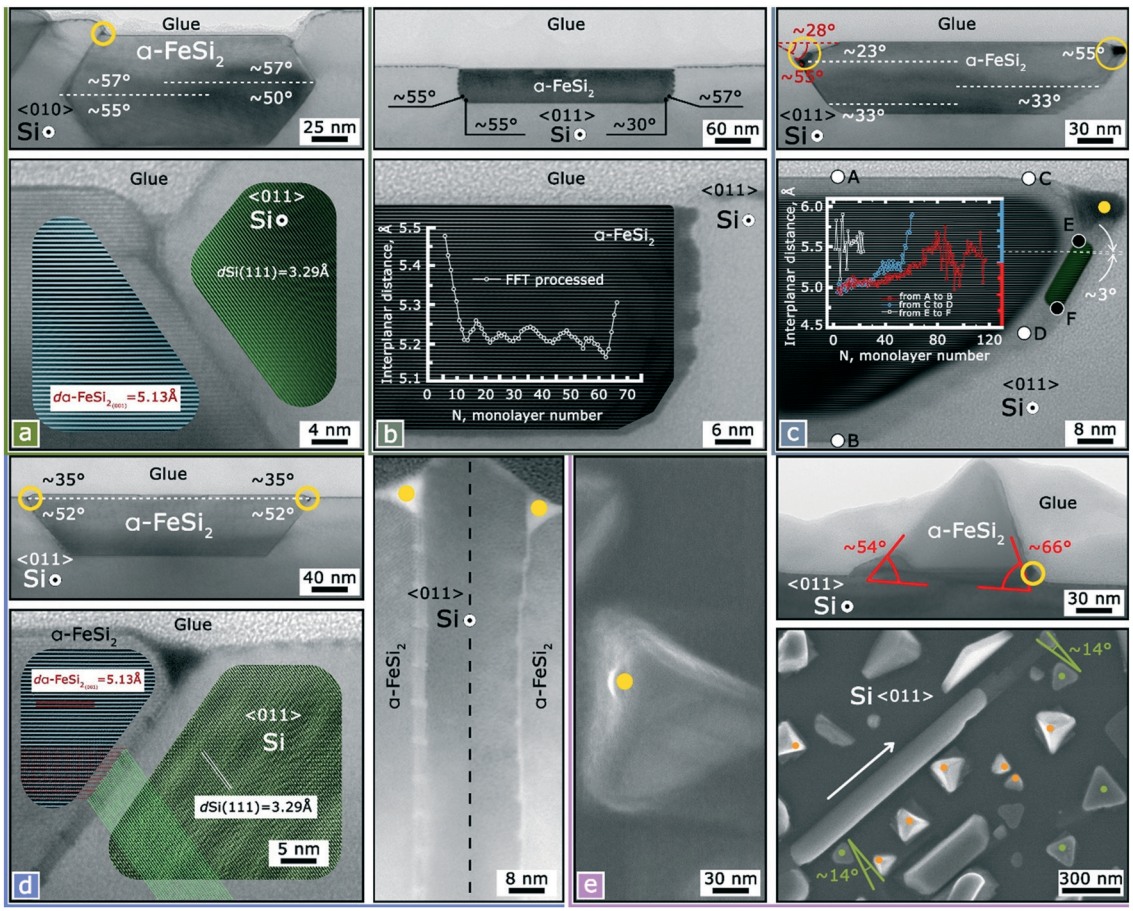

Fig. 3 TEM and SEM images of α(001)//Si(001) nanocrystals representing their various shapes obtained from the sample series discussed. (a)–(d) Depict an overview of certain rectangular and triangular α-$FeSi_2$ nanoplates and a magnified view of α//Si interfaces is also given; the right panel of (d) shows both stepped side interfaces of a nanocrystal and is presented in colour inverted form to emphasize the stepped nature of the interface. The magnified views of nanocrystals contain FFT-processed areas to highlight atomic planes. Additionally, interplanar spacing profiles are shown in (b) and (c). The profiles in (c) correspond to different sections of the nanocrystal, namely from A to B, from C to D, and from E to F. Yellow dots and circles point to presupposed zones filled with gold droplets. (e) Demonstrates TEM images of the pyramid-like nanocrystals; these nanocrystals are marked with orange dots in the SEM view, while green dots point to the triangular nanoplates.

types of such nanocrystals. One is characterised by the presence of a basement upon which the triangular nanoplates grow. Such a basement can be either silicon or another silicide orientation. The second type is endotaxial

triangular nanoplates. In the AS2 sample (the case of iron-enriched flux, v_{Si}/v_{Fe} = 0.57), only endotaxial triangular nanoplates may be detected. Both types are observable in Fig. 1a and in the magnified view in Fig. 3e, depicted with green dots. Thus, the surrounding silicon matrix in AS2 determines the strict alignment of the nanocrystal sides in AS2 samples along the Si<011> direction.

• The third one is trapezoid nanoplates inclined by ~22° relative to the Si<001> direction and placed along the Si<011> direction (Fig. 1g; yellow lines). The inherent sizes are almost the same for each trapezoid (height: 200 nm, width: 350 nm, and thickness: 30 nm) in AS1 and AS2. The trapezoids in sample S1 are smaller – height: 100–150 nm, width: 50–350 nm – but the thickness is close to 30 nm, like the nanocrystals in the AS1 and AS2 samples.

• The fourth type is polyhedral nanobars (Fig. 1a and b; pink lines) aligning along the Si<011> direction with a length of up to 1.5 μm, a width ranging between 100 and 200 nm, and a thickness of about 50–110 nm.

• The fifth type are tetrahedrons with two equal edges varying from 80 to 300 nm that are approximately 1.5 times longer than the third edge. The height varies from 16 to 170 nm (Fig. 1a and b; light blue triangles).

• The sixth type is pyramid-like nanocrystals (Fig. 1a; violet triangles) with a side length varying from 70 to 200 nm and a height of about 150 nm.

XRD patterns of the samples (Fig. 2a) reveal six basic orientations of α-$FeSi_2$ crystallites on the Si(001) substrate: 001, 111, 110, 102, 211, and 100. The sample S2 is almost mono-oriented with α(111) planes parallel to Si(001). From asymmetric φ-scans (Fig. 2b), the following epitaxial orientations have been determined: α-$FeSi_2$(001)[110]||Si(001)[110], α-$FeSi_2$(001)[110]||Si(001)[100], and α-$FeSi_2$(111)[−110]||Si(001)[110]. φ-Scans of {110} reflections (Fig. 2d) disclosed an additional orientation of α-$FeSi_2$, with the {102} planes offset by ~20.5° around the [010] (and [−110]) zone axis of the Si(001) substrate. The {102} planes of this additional orientation (denoted further as α-$FeSi_2$(102)/20.5°/Si(001)[110]) appear approximately parallel to the {110} planes of crystallites with the orientation α-$FeSi_2$(111)||Si(100). The average α-$FeSi_2$ lattice parameters and fractions of crystallites of different orientations in the samples (Table 1) were determined *via* full-profile refinements of symmetric and offset diffraction scans using the derivative difference minimisation method.[45] Therefore, one can see the strong influence of the α-$FeSi_2$ nanocrystal growth conditions on the preferred OR.

Table 1 α-$FeSi_2$ lattice parameters and fractions of crystallites of different orientations

Sample	AS1	AS2	S1	S2
Lattice parameter, Å				
a	2.6948(2)	2.6939(1)	2.6912(2)	2.6967(4)
c	5.1352(2)	5.1335(2)	5.1260(5)	5.136(2)
Fraction of orientation, %				
α(001)//Si(001)	69.1	57.7	1.4	0.3
α(111)//Si(001)	25.0	40.2	82.2	99.7
α(110)//Si(001)	0.8	0.8	0.7	—
α(102)//Si(001)	5.1	1.3	3.6	—
α(100)//Si(001)	—	—	11.7	—
α(211)//Si(001)	—	—	0.4	—

The utilisation of catalyst-free conditions changes the preferable OR from α(001)//Si(001) for the catalyst-activated Si(001) surface to an α(111)//Si(001) OR. In turn, changes in the ratio of the deposited Si/Fe flux regulate the texture level of the nanocrystal ensemble as well. Thus, increased amounts of iron in the flux in the case of the gold-activated silicon surface diminish the texture with an α(001)/Si(001) OR, whereas under the same conditions, the texture on the α(111) plane is heightened in the case of the gold-free Si(001) silicon surface.

According to the XRD results, most of the nanocrystals in the AS1 and AS2 samples should have an α(001)//Si(001) OR, and their volume fraction is changed to 11.4%. Nevertheless, SEM images (Fig. 1) clearly show that the largest fraction of surface area is filled with rectangular nanoplates in the case of the AS2 sample, whereas in the case of the AS1 sample it is filled with smaller pyramid-like nanocrystals and triangular nanoplates. Therefore, these habit types can be regarded as belonging to the α(001)//Si(001) OR. The decrease in the α(001)//Si(001) OR volume fraction observed from the AS2 sample may be caused by inequivalence in the kinetics and energies of interfaces of the α(001)//Si(001) nanocrystals with different shapes. Since a decrease in the volume fraction of the α(001)//Si(001) OR is observed, one can suggest that a tendency to accomplish $FeSi_2$ stoichiometry and form endotaxial nanoplates under an iron-rich flux is less energetically favourable than the formation of α(111)//Si(001) nanocrystals but more favourable than the formation of the pyramid-like nanocrystals massively observed on the AS1 sample synthesised under silicon-rich atomic flux.

α-$FeSi_2$(001)[010]//Si(001)[010]&[110]

Fig. 3 shows typical TEM and SEM images of nanocrystals with an α(001)//Si(001) basic OR. Atomic planes that are detectable and parallel to the Si(001) surface in TEM images give an average interplanar spacing value of 5.13 Å, which is in good correspondence with the XRD results for the α(001) interplanar distance (see the insets with fast Fourier transform (FFT) processing (Fig. 3c and d and S2, ESI†)). These nanocrystals are rectangular and triangular nanoplates and pyramid-like nanocrystals. Fig. 3a–d shows cross-section TEM images of some nanoplates. It is notable that the larger interface area between α-$FeSi_2$ and Si for all nanocrystals discussed is formed by flat α(001) and Si(001) planes, while side interfaces vary from one specimen to another. Still, there could be some deviation from the α(001)//Si(001) OR. One can notice that the bottom of the pyramid-like nanocrystals is not parallel to the Si(001) plane and is deflected by ~5° (Fig. 3e, upper panel). Moreover, such inclination of the main interface is detectable in the rectangular and triangular

nanoplates. This can vary in range from 2.8 to 9° (Fig. S2, ESI†). In turn, observable angles between the α(001) plane and the α||Si side interfaces lie in the range from 22° up to 70° (Fig. S3, ESI†). This variety of angles detected can be explained both through the existence of multiple α-$FeSi_2$ planes forming low-energy interfaces with certain silicon planes and based on projections that appear in the case of TEM measurements. Three different types of interface can be distinguished among the side facets observed. They are flat ones, as in Fig. 3a, stepped ones, as in Fig. 3d, and stressed α(001) planes deviating by 2–3° (Fig. 3c, the FFT processed area with edges denoted by E and F, and Fig. S2, ESI†). The interplanar spacings for these planes appear larger than the α-$FeSi_2$ bulk values and demonstrate a value close to 5.5 Å (Fig. 3c, E–F). Moreover, the α(001) planes, which are located near the edges, at the top and bottom of the nanoplates indicate lattice strain as well (Fig. 3b and c (points A–B and C–D), and S2, ESI†). The interplanar spacing gradually decreases from 5.5 to 5.13 Å while moving from the edges to the centre.

It worth noting that, according to theoretical findings by N. Zamkova and V. Zhandun, changes in the α-$FeSi_2$ lattice parameters induced by non-stoichiometry or epitaxial lattice strain may lead to ferromagnetism.[31,46] Analysis of SEM images from the sample series showed that rectangular and triangular nanoplates grow only on gold-activated silicon surfaces (Fig. 1 and S1, ESI†). Hence, gold droplets play a key role in their formation. Looking through the TEM images

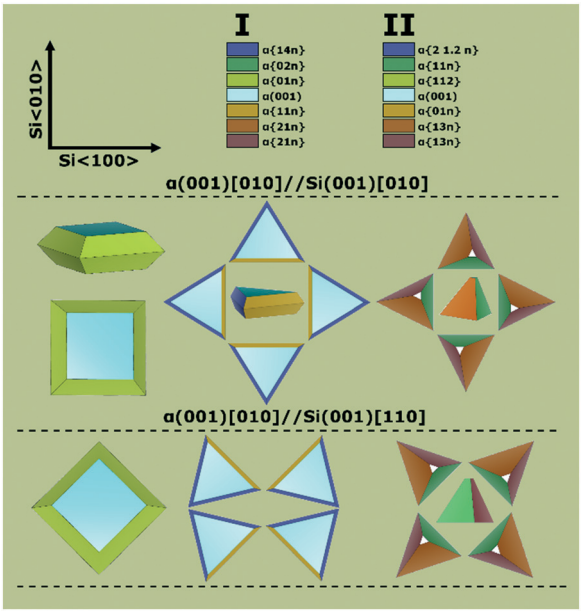

Fig. 4 An illustrative scheme to represent the variety of faceting of the α(001)//Si(001) nanocrystals grown. Their spatial alignment is given according to experimental observations. The coordinate axes in the upper-left corner establish the parallelism of the facets to the silicon directions. Possible facets for two cases of epitaxial alignment, α-$FeSi_2$(001)[010]||Si(001)[010]&[110], are marked with different colours. For example, eventually, for rectangular nanoplates, four side facets are possible: α{01*n*}||Si{01*n*}, α{01*n*}||Si{11*n*} and α{11*n*}||Si{11*n*}, and α{11*n*}||Si{10*n*}.

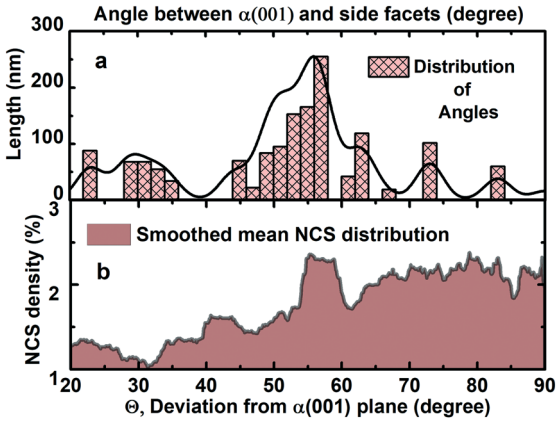

Fig. 5 The distribution of observable angles in the experimental TEM images between α(001) and the side facets of the α(001)//Si(001) rectangular and triangular nanoplates as a function of the length of their projections on the TEM image plane (a). Smoothed mean NCS density calculated for side interfaces possible for the α(001)[010]//Si(001)[110],[010] basic ORs and plotted as a function of angle between the side interface and α(001) plane (b).

(Fig. 3), it is possible to detect areas darker than those corresponding to α-$FeSi_2$ silicide. Such areas are marked with yellow circles and dots. In most cases, gold is situated at the corners of the tops of the nanocrystals. Thus, gold in droplet form in the initial growth stages can induce the formation of certain α-$FeSi_2$ planes and spread over the edge facets during synthesis. Surface EDX analysis showed that gold is homogeneously spread over the whole sample surface at a nominal gold thickness of 1 nm (Fig. S4, ESI†); one can find additional data (Fig. S5–S8†) and discussion about the influence of gold on nanocrystal growth in the ESI.† In turn, all three types of α(001) nanocrystal (triangular and rectangular nanoplates, and pyramid-like nanocrystals) are aligned with either Si[010] or Si[110]. The rectangular nanoplates have their side facets aligned along Si[010] or Si[110]. Then, two types of α-$FeSi_2$ facets are possible for each OR, *i.e.* created by α{01*n*} or α{11*n*} planes (Fig. 4). Therefore, four side interfaces can be formed, which are α{01*n*}||Si{01*n*}, α{01*n*}||Si{11*n*} and α{11*n*}||Si{11*n*}, and α{11*n*}||Si{10*n*}. Possible planes of facets for triangular nanoplates and pyramid-like nanocrystals were also determined, taking into account the angles between the side facets and Si<110> directions, and are shown in Fig. 4. Triangular nanoplates (depicted with green dots in Fig. 3e) with observable angles of ~61° (two obtuse angles) and ~59° (an acute angle) show one side deviating from the Si<110> direction by ~14°. The only planes with this type of direction that can have such a deviation value in the case of the α(001)//Si(001) OR are α{14*n*} and α{21.2*n*} for both α[010]//Si[010] and α[010]//Si[110] azimuthal alignment. Fig. S9, ESI,† shows a schematic illustration of the possible spatial alignment of the α-$FeSi_2$(001)//Si(001) triangular nanoplates.

According to Fig. 3e, the pyramid-like nanocrystals are not endotaxial and do not have a large side interface with silicon. The angles between α(001) and its free side facets are ~54°

and ~66° (Fig. 3e and S1, ESI†). The angles of the triangular projections formed by the pyramid-like nanocrystals are ~64° for the two angles and ~54° for the other one. A top view of the pyramid-like nanocrystals (Fig. 3e, depicted with an orange dot) reveals the asymmetric slope of the two side facets that form an acute angle (~54°); therefore, the two others are at ~63°. From this data, the most appropriate planes to describe the habit that appears are α{21*n*} and α{13*n*} for both the α[010]//Si[010] and α[010]//Si[110] azimuthal alignments observed (Fig. 4). Atomistic illustrations of the pyramid-like nanocrystals with specific α(−2−1−1), α(2−12), and α(011) facets under different projections are given in Fig. S10a–d, ESI.† Additionally, triangular projections with two angles of 63.44° and a third one of 53.13° and formed by the intersected planes α{110}, α{130}, and α(010) or α(210) are given for visualisation purposes in Fig. S10e and f, ESI,† respectively.

The varieties of faceted shapes of the α(001)//Si(001) nanocrystals and their interface morphologies are caused by good matching between silicon and silicide planes, and also by close-packed atomic rows in these compounds. We also attempt to find out the origin of the interface formation and faceting of the α(001)//Si(001) triangular and rectangular nanoplates from the view of the NCSs between Si and α-$FeSi_2$ compounds. A detailed consideration of the NCS densities of possible side interfaces for the α(001)//Si(001) triangular and rectangular nanoplates shows that the distribution of observable angles in experimental TEM images between α(001) and their side facets (Fig. 5a) and the mean smoothed NCS distribution line are in good accordance. The maximum observed at around 55 degrees on the experimental curve (Fig. 5b) is supposed to be due to the high NCS density of the α(112) and α(447) planes for the α(001)[010]//Si(001)[010] basic OR (see calculation details and additional discussion in the ESI†). Thus, we conclude that the side interfaces of the rectangular and triangular nanoplates are mainly created from α(112)||Si(111) or α(112)||Si(302) habit planes for the α(001)[010]//Si(001)[010] and α(001)[010]//Si(001)[110] basic ORs.

The α(112) and Si(111) or α(112) and Si(302) planes are not parallel under the condition of the parallelism of basic interfaces for the α(001)[010]||Si(001)[010]&[110] ORs. As in the example of the α(001)[010]||Si(001)[010] OR, the α{112} and Si{111} planes are not parallel, even though their parallelism could bring about a high side facet NCS density value. The angle between these planes is 1.244°. As noted above, a TEM examination of the side facets of the α(001)//Si(001) nanoplates reveals lattice stress at the edges. Other pairs of silicide {01*n*} or {11*n*}||silicon {01*n*} or {11*n*} planes, which may be side interface candidates for the nanoplates show no parallelism in the case of the α(001)[010]||Si(001)-[010]&[110] basic ORs. The typical deviation varies in the range of 3° (Table S3†), which is in correspondence with the TEM experimental data (Fig. 3d and S2, ESI†).

Indeed, analysis of the NCS densities of stressed and unstressed side interfaces reveals that under stressed conditions, the NCS density increases (Fig. 6a). In the case of

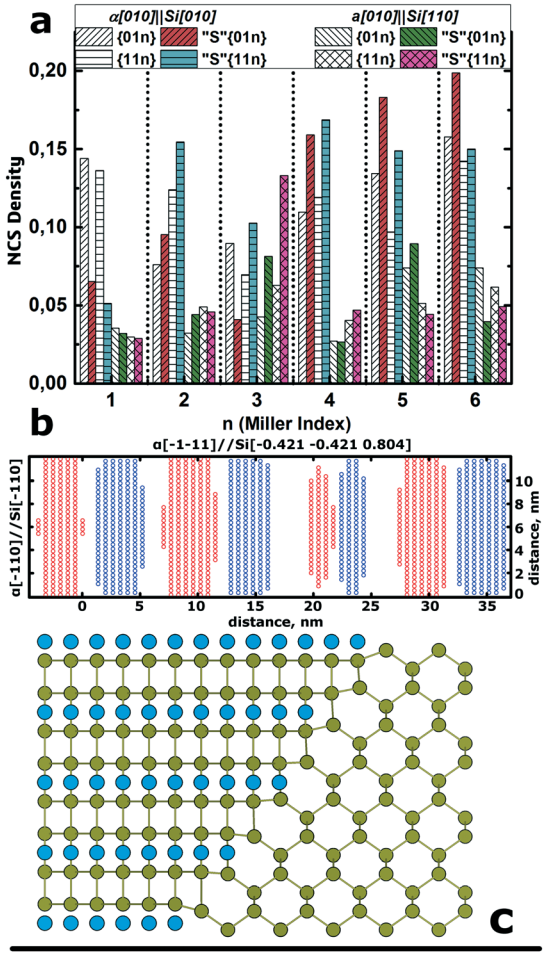

Fig. 6 (a) A comparison of NCS density values between stressed (denoted as "S") and unstressed possible side interfaces of α(001)//Si(001) nanoplates for both the experimentally observed azimuthal alignment α[010]//Si(010) and α[010]//Si[110]; *n* denotes the Miller index for the α-$FeSi_2${01*n*} or {11*n*} planes. (b) An NCS distribution map in the case of α(112)||Si(111) non-stressed side interfaces for rectangular nanoplates with α(001)[010]||Si(001)[010] OR. (c) An atomistic representation of the α(112) or α(447)||Si(111) interface.

the α(001)[010]//Si(001)[010] basic OR, the NCS density of interfaces formed by α{11*n*} planes is raised for all values of *n* taken into account, except for *n* = 1. When *n* = 1, the NCS densities for both the α{11*n*} and α{01*n*} interfaces become smaller than in the case of the unstressed interfaces. It is expected that the α{111} and α{011} interfaces should be abrupt. This additionally supports the suggestion that for most values of n, the α{11*n*} planes prefer to form during growth on the side facets due to the higher NCS density in comparison with the α{01*n*} planes. In turn, the α(001)[010]||Si(001)[110] OR is inferior in this respect and is expected to result in the formation of rectangular nanoplates. This also supports the idea put forward above that the α(001)[010]||Si(001)[110] OR corresponds to the triangular nanoplates or pyramid-like nanocrystals. The only NCS density obtained for α(001)[010]||Si(001)[110] that is higher than the α(001)[010]||Si(001)[010] counterpart is the {113}

plane with an angle of 42° with respect to α(001). This angle is rarely observed in the TEM images (Fig. S3, ESI†).

Moreover, the α{112}||Si{111} interface is suggested to be stepped (Fig. 3d, θ = ~52°). The calculation of the NCS distribution map for this non-stressed interface between two neighbouring α(112) layers with an α(001)[010]||Si(001)[010] OR reveals that the side interface may also be stepped rather than planar. The NCS distribution map at two neighbouring α{112} layers is shown in Fig. 6b. The NCS distribution map from the single α{112} plane (blue circles) gives an NCS percentage of about 35% (with the NCS criterion of 1.1 Å). As shown in Fig. 6b, the NCSs on the successive layer (red circles) of the α{112} plane connect with the previous one, so the NCS percentage of such an interface improves to about 70%. The length of a typical terrace at this α{112}||Si{111} interface is about 5 nm, which is similar to the interface deviation observed from the experimental TEM images (Fig. 3d).

As has already been noticed, a high NCS density for the side interfaces of rectangular nanoplates is observed for the α(112) and α(447) planes (Fig. S11, ESI†). These planes deviate from each other by a small angle of ~3.6°. Thus, the main characteristic of the epitaxial ordering of both the α(112)||Si(111) and α(447)||Si(111) interfaces should be similar. Namely, silicon atoms from the silicide lattice tend to create bonds with those in the Si(111) plane (Fig. 6c). Phenomena such as the formation of steps on the interface (Fig. 3b) and the appearance of stressed planes (Fig. 3c) promote the repeating of this pattern over as large an area as possible. The energetic favourability of the formation of the α(112)||Si(111) OR is confirmed by frequent observations during the formation of the α-$FeSi_2$ phase on/into silicon.[9,47,48]

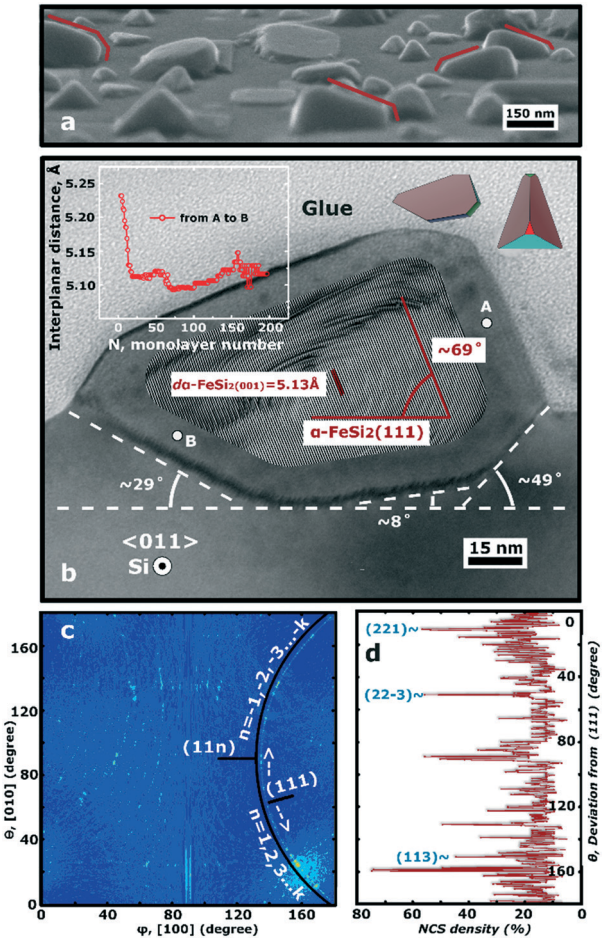

Fig. 7 SEM (a) and TEM (b) images of α(111)//Si(001) nanocrystals; the inset in (b) depicts the interplanar distance between α(001) planes from A to B, (c) the NCS density map for the α(111)//Si(001) basic OR. (d) The NCS density distribution line obtained at rotation around the α[−110] direction starting from the α(111) plane (the surface area utilised for calculations is 120 × 120 Å and the step interval is 0.5°).

α-$FeSi_2$(111)[−110]//Si(001)[110]

The aspect ratio from the top view of a triangular projection of the tetrahedrons is about 1.5, corresponding to the ratio between the sides formed from the α(111) plane in the α-$FeSi_2$ unit cell (Fig. 1, blue triangles). Cross-section TEM images of this tetrahedron reveal that the α(001) planes detectable are situated at an angle of 69 degrees with respect to the Si(001) surface, which is in good correspondence with α(001) < α(111) = 69.69°. One can see that the tetrahedrons have identical faceting and that their typical form is a complex polyhedron (Fig. 7a and b). Comparatively with the α(001)//Si(001) nanoplates, the lattice stress of about 2.5% is only detectable on facets that are in the contact with the vacuum (Fig. 7b, point A). Another side adjacent to silicon shows no lattice stress (Fig. 7b, point B). It is also worth noting that gold is not observed at the edges, so one can conclude that it does not affect the formation process of the α(111)//Si(001) nanocrystals.

Fig. 7c represents the NCS density plotted as a function of the rotation angles φ and θ, which correspond to rotation around the α[010] and α[100] directions in the α-$FeSi_2$(111)[−110]//Si(001)[110] heterostructure, respectively. It reveals scant spots of high NCS density. Mostly they are distributed along the line corresponding to rotation around the α[−110] direction, *i.e.*, the planes with high NCS densities are the α(11*n*) ones. One can see that the α(111) plane shows a low NCS density, thus interfaces with α(111)||Si(001) planes are hardly able to be created (Fig. 7c). In turn, other planes, including α(221), α(112) and α(113), show a high value of NCS density, which may result in the growth of nanocrystals towards the silicon substrate along these planes. The angles observable between the α(111) plane and silicon||silicide interface, which are 29°, 8° and 49°, correspond to planes with a high NCS density, α{113}, α{221} and α{22−3}, respectively (Fig. 7d). This complex interface for the basic α(111)//Si(001) OR is detectable in both cases with and without the use of gold, which sheds light on the structures and morphological characteristics of α(111)//Si(001) thin films.[32] The crystal shapes of the α(111)//Si(001) nanocrystals depicted in the inset of Fig. 7b were constructed using the

planes determined *via* NCS analysis and replicate the shape observable experimentally.

α-$FeSi_2$(102)[100]//Si(001)[110]

The high aspect ratios of the polyhedral nanobars (10–15) may be due to the high anisotropy of the NCS distribution over the interface, which results from anisotropy of lattice mismatch between silicon and α-$FeSi_2$ compounds. Analysis of TEM images (Fig. 8b) indicates correspondence between the polyhedral nanobars and the α-$FeSi_2$(102)[100]// Si(001)[110] OR. The α(001) planes are inclined with respect to the Si(001) surface by ~43.7°, and α(102) < α(001) = 43.69°. It is easily noticeable that the α-$FeSi_2$(102)//Si(001) nanobars have a stepped interface caused by an increase in the NCS density along the α[021] direction through three neighbouring α(102) layers (Fig. 8c). Anisotropic growth resulted from an NCS pattern with a high NCS density spread along the α[100] direction. As one can notice, the NCS density of the α-$FeSi_2$(102)||Si(001) habit plane is about 10% (Fig. 8d, Θ = 0), while the creation of a stepped interface increases this parameter threefold, making it comparable with the high NCS density values at other Θ angles.

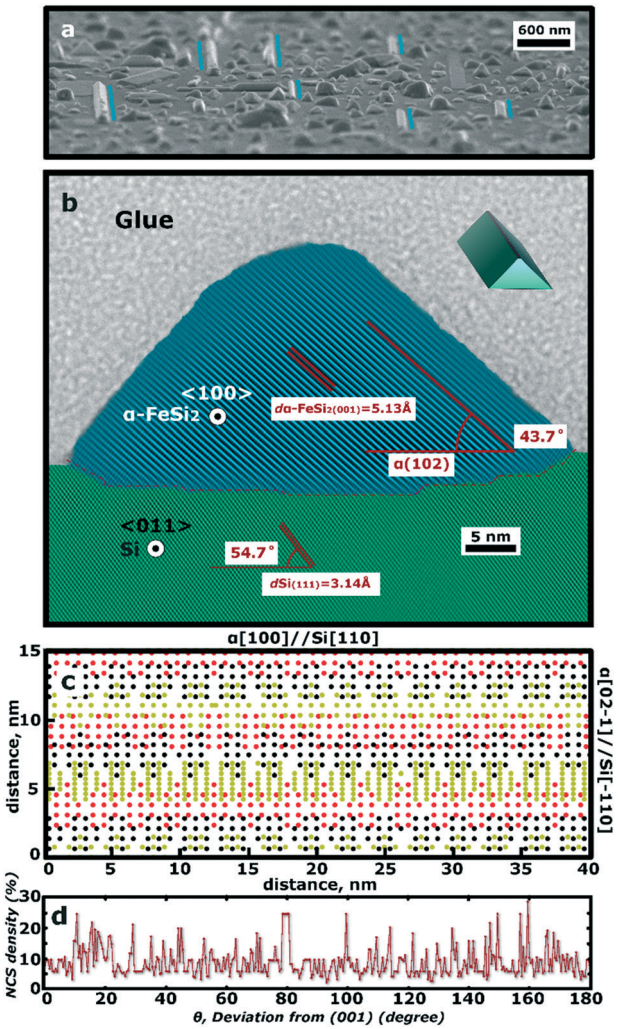

Fig. 8 SEM (a) and TEM (b) images of α(102)//Si(001) nanocrystals. (c) The NCS distribution map at the α(102)||Si(001) interface for polyhedral nanobars with an α(102)[100]||Si(001)[110] OR; the different colours depict the NCSs in three different neighbouring α(102) layers, illustrating the origin of the stepped interface. (d) The NCS density distribution line obtained upon rotation around the α[100] direction starting from the α(102) plane (the surface area utilised for calculations is 120 × 120 Å and the step interval is 0.5°).

α-$FeSi_2$(102)/20.5°/Si(001)[110]

Fig. 9a and b presents SEM and TEM images of the trapezoid nanoplates. It is noticeable that the α(001) planes are situated at ~67° relative to the Si(001) plane, whereas α(102) is tilted by ~23°. These findings indicate that the plane parallel to Si(001) is *a* plane with a high Miller index, which is not detectable by the XRD method. Thus, we can assign the α-$FeSi_2$(102)/20.5°/Si(001)[110] OR to the trapezoid nanoplates. Their formation process has a distinctive feature. The silicide||silicon interface here reveals the presence of a buffer layer between the silicon substrate and the standing

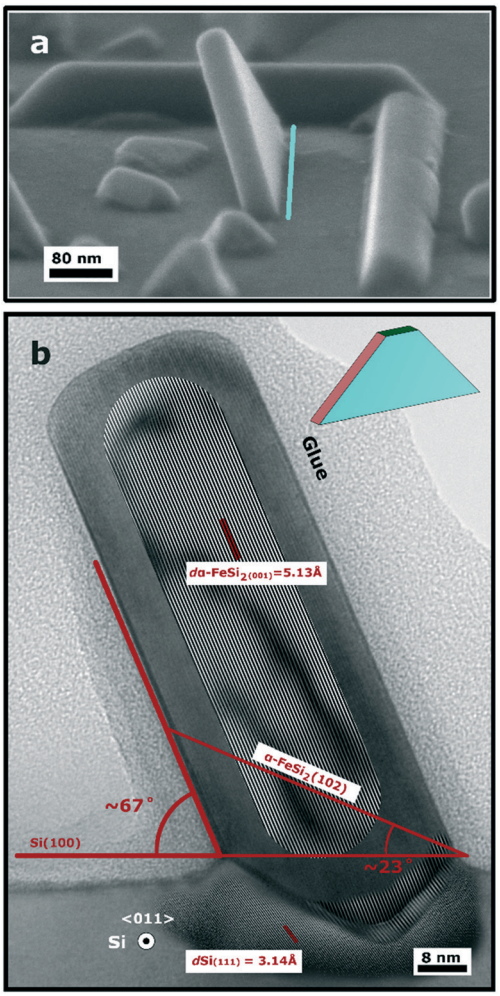

Fig. 9 SEM (a) and TEM (b) images of α-$FeSi_2$(102)/20.5°/Si(001) triangular trapezoids.

trapezoid nanoplate. Atomic planes in this buffer layer are strongly stressed if the α-$FeSi_2$ compound is considered. The α(001) interplanar spacing, in this case, is larger by 11.4% (5.72 Å). Thus, the buffer layer plays a key role in the formation of such an exotic OR and this type of α-$FeSi_2$ nanocrystal.

Growth mechanism discussion

The planes distinguishable in the buffer layer appear parallel to Si(111) (Fig. 9b and S15a, ESI†), whereas the (001) planes in the trapezoid nanoplates are slightly inclined by 4°. Hence, we may suggest that a critical island initially forms an interface so that the (001) and Si(111) planes are parallel. Consequently, this embedded nanoisland becomes stressed to accomplish the favourable epitaxial conditions. The interplanar distance between the (001) planes formed by only silicon atoms according to experimental data is about 3.1 Å, which is close to the Si(111) interplanar distance (d = 3.14 Å). While growing, such tension becomes more and more unfavourable so that a newly orientated phase appears.

It is interesting to note that despite the Fe-rich flux conditions, this type of nanocrystal does not grow endotaxially (Fig. 1b, yellow lines); on the contrary, it grows away from the substrate. This indicates that the stressed buffer layer may block nanocrystal growth towards the substrate due to a low iron atom diffusivity rate. Then, the required amount of silicon atoms to accomplish $FeSi_2$ stoichiometry is provided by atoms that come to the top of the trapezoid nanoplates from the surrounding area (Fig. 10a). The buffer layer restricts the lateral growth of the trapezoid nanoplates so that all nanoplates have an almost identical lateral size of about 30 nm (Fig. 9). The incapability of the stressed buffer layer to spread further with the (001)// Si(111) OR due to a volume energy penalty impels the buffer layer to adopt a finite size, while the newly forming trapezoid nanoplates aim to extend the area of the energetically favourable (001) plane (Fig. 10a).

The experimental findings discussed above clearly show that the gold droplets preliminary deposited onto the silicon surface play a key role in the growth of the α-$FeSi_2$ nanocrystals and the development of their shapes and ORs. We suggest that during the initial stages of growth, the silicide nanocrystals form according to a vapor–liquid-crystal mechanism, like in the case of the growth of semiconducting nanowires (Fig. 10b). It is known that catalyst particles have an effect of the activation of nanowire growth based on the fact that growth on the surface under a droplet proceeds much faster than on a non-activated surface.[44] Here, the transition of material from vapour to liquid takes place and, consequently, the solution becomes supersaturated and crystallises on the surface under a droplet. As regards the growth of the α-$FeSi_2$ phase, this may also result in the formation of a particular orientation of silicide nanocrystal inside the gold droplet. The supersaturated alloy of silicon, gold, and iron may change the surface energies of adjacent facets of the α-$FeSi_2$ phase, making them more favourable from the point of view of surface energy. However, under certain conditions, lateral growth can be faster than vertical growth.[44] The physical cause of the lateral growth initiation is a decrease in diffusive flux from the substrate surface to the nanocrystal top, and an increase in supersaturation on the side facets. Consequently, the gold catalyst droplets become overgrown and the silicide nanocrystals start to create a new facet adjacent to the vacuum, which is more favourable (Fig. 10b). Thus, the (001)//Si(001) rectangular and triangular nanoplates, non-existent under the gold-free growth conditions (Table 1 and Fig. 1), are formed. Here, side facets are mostly formed by the α{112} planes, which is also demonstrated with the help of NCS density analysis at

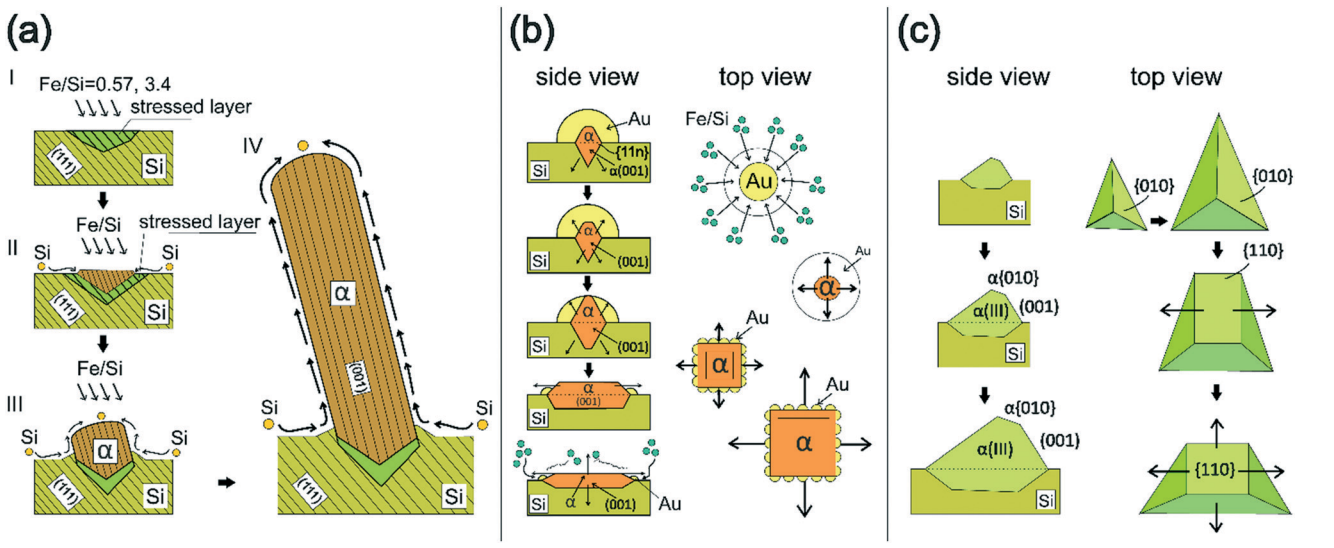

Fig. 10 A schematic illustration of the growth process of (a) the α(102)/20.5°/Si(001) trapezoid nanoplates, (b) the α(001)//Si(001) rectangular nanoplates, and (c) the α(111)//Si(001) nanocrystals.

interfaces with silicon.[22] It is also worth noting that excess gold on the nanoplate edges may result in the rounding of the nanocrystals (Fig. 1b and S5 and S7, ESI†). The edges of the nanoplates cannot overgrow the gold droplets here due to its big initial volume. This phenomenon is suggested to illustrate what is taking place in the initial stages of the growth of well-faceted nanoplates. {11*n*} or {01*n*} facets start developing when the gold droplets are overgrown (Fig. 10b).

Other gold-initiated (001)//Si(001) nanocrystals are pyramid-like ones. They are absent under gold-free growth conditions (Fig. 1). Moreover, one can trace gold droplets on their edges in TEM images (Fig. 3e). They usually grow away from the substrate on the silicon basement under gold-assisted conditions with Si-enriched flux. In turn, iron-rich flux results in their disappearance (Fig. 1) due to the endotaxial growth of the nanocrystals becoming predominant. The size of the gold droplets and silicon surface defects, along with the buffer layer between the pyramid and silicon, may also affect their formation. Additionally, any further increase in the preliminary gold layer deposition thickness results in the disappearance of this type of nanocrystal, while rectangular and triangular nanoplates are predominantly formed (Fig. S5, ESI†). Hence, one can conclude that the gold droplet size is crucial for the formation of the (001)//Si(001) pyramid-like nanocrystals.

Concerning the silicon-rich flux and large gold droplets on the silicon surface, silicon atoms incoming onto the surface tend to form large truncated pyramids (Fig. S5, ESI†) that are homogeneously distributed over the substrate. The capture of silicon atoms for the formation of truncated silicon pyramids may occur due to Oswald ripening as well. As a result, we do not observe well-shaped and faceted α-$FeSi_2$ pyramid-like nanocrystals. In response to the suggestion that a silicide critical island, corresponding to the pyramid-like nanocrystals, is equally as likely to be formed as the other gold-assisted nanocrystals that are grown, we can conclude that their appearance is suppressed due to a lack of silicon atoms that overgrow the larger gold droplets (the condition of an increased amount of gold in relation to the deposited Fe/Si) to form a well-faceted pyramid-like nanocrystal habit. The facets adjacent to the vacuum of the pyramid-like nanocrystals (α{211}, α{212} and α{011}, Fig. S10, ESI†) should be energetically less favourable than, for instance, the α(001) surface of the nanoplates prevalent under gold-rich conditions (Fig. S5, ESI†).

The growth of the nanoplates is promoted by the additional flux of silicon atoms from the silicon substrate, whereas this source of silicon atoms in the case of the growth of the pyramid-like nanocrystals under gold-rich conditions may be suppressed by the presence of a stressed buffer layer, as in the case of the α(102)/20.5°/Si(001) trapezoid nanocrystals (Fig. 9 and S15a, ESI†). Thus, one could expect the appearance of the pyramid-like nanocrystals if the deposition was not be stopped at the levels of Si–Fe discussed in this paper, on the condition that the nanocrystals would not reach the coalescence stage earlier. This question still remains rather complex and requires further investigation.

The local absence of gold droplets on the substrate surface causes the formation of the (111)//Si(001) nanocrystals (Fig. 10c), where the faceting and growth process is regulated by planes with well-developed NCS patterns, *i.e.* interface and surface energy dependent. When the Si–Fe atomic flow has the proper stoichiometry of $FeSi_2$ (v_{Si}/v_{Fe} = 3.4), the α-$FeSi_2$ nanocrystals tend to grow away from the silicon substrate and show a well-faceted morphology. The shape of the α(111)//Si(001) nanocrystals does not change under gold-assisted and gold-free growth conditions (Fig. 1a and e) due to the fact that gold is not involved in the formation process. In the case of the gold-assisted conditions, there is still a silicon surface not covered by gold droplets where the α(111)//Si(001) nanocrystals can form. However, with a further increase in the amount of gold deposited, this nanocrystal type becomes less observable (Fig. S5, ESI†). Growth conditions with Fe-enriched flux affect the formation process of the α(111)//Si(001) nanocrystals as well. As can be seen in Fig. 1, the gold droplets affect the diffusion paths of atoms for attracting new atoms from nearby, along with the preferred growth of the nanoplates. The absence of such diffusion anisotropy caused by gold leads to the formation of uniformly distributed α(111)//Si(001) nanocrystals, which are partially coalesced and show poorly faceted morphology (Fig. 1f and h).

It is worth summarising the lattice strain observed in the α-$FeSi_2$ nanocrystals grown. Direct observations of the distortion of the α(001) planes from TEM images indicate that the volume corresponding to the distorted lattice should not exceed 20 and 8% of the total volume for the nanoplates and tetrahedrons, respectively (Fig. 3 and 8). The distortion of the α(001) planes is about 5%, which is comparable with the interplanar spacing misfit between the α(001) and Si(001) planes (−5.57%). For other types of nanocrystals, the distortion of α(001) is less noticeable (Fig. 8 and 9). The α(001) distortion may be caused not only by misfit between the silicon substrate and silicide; the lattice stress observed in the nanocrystals is a complex problem where different factors are involved, including inherent vacancies in the iron atom sheets, the relaxation of the surface adjacent to the vacuum, and further air oxidation.

The interplanar distances corresponding to the main ORs were estimated for comparison with those known in the literature to assess the lattice strain caused by epitaxial alignment (Table S5, ESI†). The α-$FeSi_2$ lattice parameters were separately refined based on a set of diffraction reflections corresponding to the nanocrystal type given. As one can see, the misfits for the lattice parameters and interplanar spacings determined are mainly less than 1%, which is in the range of the discrepancy observed for the α-$FeSi_2$ lattice parameters reported in the literature (Table S4,[29,49] ESI†). Thus, the observation of possible lattice strain in the nanocrystals is hindered by the increasing impact of

the bulk properties due to relatively large size of the α-$FeSi_2$ nanocrystals discussed in this work (Fig. 1 and 3–9).

However, some distinctive increase in the interplanar spacing misfit is observed for the α{114} plane corresponding to the α(001)//Si(001) nanocrystals (Table S4, ESI,† nanoplates and pyramid-like nanocrystals). It has values of about −8.5% in comparison with the values for α{114} planes known in the literature. Thus, the estimated epitaxial strain[22,50] of 1.01% (Table S5, ESI†) for the α(001)[010][49]||Si(001)[010] OR reduces down to 0.32 ± 0.17% according to the interplanar distances determined from the diffraction peaks corresponding to the α(001), α(002), α(003), α(004), and α{114} planes (Table S4, ESI† and Fig. 2). In the case of α(111)[−110][49]||Si(001)[110], the lattice parameters determined with the use of the α(111) and α{110} reflections for the S1 and S2 samples indicate an increase in the lattice strain of 1.34 ± 0.21% (S1) and 0.96 ± 0.06% (S2) in comparison with the estimated value of 3.01% (Table S5, ESI†). Nevertheless, the interface strain for the tetrahedrons decreases down to 2.45 ± 0.19% in comparison with the estimated value (Table S5, ESI†). The difference in the lattice stress for the same OR may be caused by different morphologies of α(111)//Si(001) nanocrystals. The α(111)//Si(001) tetrahedrons do not have an interface with the α(111) plane parallel to the Si(001) one, whereas the poorly faceted α(111)//Si(001) nanocrystals (Fig. 1) corresponding to the S1 and S2 samples show an α(111)||Si(001) interface (Fig. S17, ESI†), where atomic reconstruction is expected to make this interface more favourable.

Conclusions

Tuning preferable ORs and shapes of free-standing α-$FeSi_2$ micro/nanocrystals has been demonstrated with the help of gold-assisted and gold-free growth conditions, additionally in conjunction with Si/Fe atomic flux alterations, on the same silicon Si(001) surface *via* molecular beam epitaxy. Thus, gold plays a deterministic role in the formation of a preferred OR between the nanocrystals and silicon substrate, while the Si/Fe flux ratio allows us to tailor a preferred nanocrystal morphology with the same basic OR. The amount of gold preliminarily deposited onto the silicon surface strongly changes the quantity of free-standing α-$FeSi_2$ nanocrystals that grow. At the same time, it regulates their aspect ratio and lateral size distribution. The size of the gold droplets may affect the morphologies of the nanocrystals as well. The variety of forms and preferable orientations that it is possible to grow on Si(001) is enriched by good lattice correspondence between silicon and the α-$FeSi_2$ compounds. The interfaces for one type of α-$FeSi_2$ nanocrystal, namely the α(001)//Si(001) nanoplates, show diversity due to several options for energetically favourable interfaces with high NCS densities. They are: (i) stressed α(001); (ii) stepped α{112}; and (iii) flat α{11*n*} and {010} planes.

The information obtained is crucial for understanding the formation process of α-$FeSi_2$ nanocrystals and it can be used to develop silicide/silicon heterostructure designs and engineer their physical properties for practical applications. Lattice stress may lead to ferromagnetism; in turn, the morphologies of interfaces may regulate leakage current and Schottky barriers in electric contact with silicon.[26,27] Such α-$FeSi_2$-based building blocks can be utilised for the further growth of ferromagnetic, topological insulator layers[51] and silicon nanowires[52] on silicon surfaces to obtain appropriate lattice stress, or they could be nucleation centres for the creation of pits in a silicon surface, which consequently may be developed in a particular way *via* anisotropic etching.

Conflicts of interest

There are no conflicts to declare.

Acknowledgements

The experimental part of the reported study was funded by the Russian Science Foundation, project no. 16-13-00060-П. Theoretical analysis of the ORs of the α-$FeSi_2$ nanocrystals grown was supported by the Russian Foundation for Basic Research, Government of Krasnoyarsk Territory, Krasnoyarsk Regional Fund of Science *via* research project No. 18-42-243013. We also acknowledge the Krasnoyarsk Regional Center of Research Equipment of Federal Research Center "Krasnoyarsk Science Center SB RAS" for support with carrying out the microscopic investigations. I. A. Tarasov personally thanks M. A. Visotin for continuous fruitful discussion about the energetics of the formation of the α-$FeSi_2$ nanocrystals.

References

1 D. Li, C. Lan, A. Manikandan, S. Yip, Z. Zhou, X. Liang, L. Shu, Y.-L. Chueh, N. Han and J. C. Ho, *Nat. Commun.*, 2019, **10**, 1664.
2 Y. Nakamura, S. Amari, N. Naruse, Y. Mera, K. Maeda and M. Ichikawa, *Cryst. Growth Des.*, 2008, **8**, 3019–3023.
3 D. Z. Chi, *Thin Solid Films*, 2013, **537**, 1–22.
4 D. B. Migas and L. Miglio, *Phys. Rev. B: Condens. Matter Mater. Phys.*, 2000, **62**, 11063–11070.
5 N. G. Galkin, D. L. Goroshko, V. O. Polyarnyĭ, E. A. Chusovitin, A. K. Gutakovskiĭ, A. V. Latyshev and Y. Khang, *Semiconductors*, 2007, **41**, 1067–1073.
6 H. Tokushige, T. Endo, K. Hiidome, K. Saiki, S. Kitamura, T. Katsuyama, N. Ikeda, Y. Sugimoto and Y. Maeda, *Jpn. J. Appl. Phys.*, 2015, **54**, 07JB03.
7 Z. Liu, S. Wang, N. Otogawa, Y. Suzuki, M. Osamura, Y. Fukuzawa, T. Ootsuka, Y. Nakayama, H. Tanoue and Y. Makita, *Sol. Energy Mater. Sol. Cells*, 2006, **90**, 276–282.
8 M. Mohebali, Y. Liu, L. Tayebi, J. S. Krasinski and D. Vashaee, *Renewable Energy*, 2015, **74**, 940–947.
9 S. Sakane, T. Ishibe, T. Hinakawa, N. Naruse, Y. Mera, M. Mahfuz Alam, K. Sawano and Y. Nakamura, *Appl. Phys. Lett.*, 2019, **115**, 182104.
10 J. Theis, R. Bywalez, S. Küpper, A. Lorke and H. Wiggers, *J. Appl. Phys.*, 2015, **117**, 054303.

11 D. Leong, M. Harry, K. J. Reeson and K. P. Homewood, *Nature*, 1997, **387**, 686–688.
12 Y. Maeda, K. Umezawa, Y. Hayashi and K. Miyake, *Thin Solid Films*, 2001, **381**, 219–224.
13 A. Kumar, G. K. Dalapati, H. Hidayat, F. Law, H. R. Tan, P. I. Widenborg, B. Hoex, C. C. Tan, D. Z. Chi and A. G. Aberle, *RSC Adv.*, 2013, **3**, 7733.
14 Y. Maeda, T. Tatsumi, Y. Kawakubo, Y. Noguchi, H. Kobayashi, K. Narumi and S. Sakai, *Phys. Status Solidi C*, 2014, **11**, 1626–1629.
15 A. V. Shevlyagin, D. L. Goroshko, E. A. Chusovitin, S. A. Balagan, S. A. Dotcenko, K. N. Galkin, N. G. Galkin, T. S. Shamirzaev, A. K. Gutakovskii, A. V. Latyshev, M. Iinuma and Y. Terai, *J. Appl. Phys.*, 2017, **121**, 113101.
16 Y. Nakamura, Y. Nagadomi, S.-P. Cho, N. Tanaka and M. Ichikawa, *Phys. Rev. B: Condens. Matter Mater. Phys.*, 2005, **72**, 075404.
17 Y. Nakamura, Y. Nagadomi, S.-P. Cho, N. Tanaka and M. Ichikawa, *J. Appl. Phys.*, 2006, **100**, 044313.
18 H. Yamane and T. Yamada, *J. Alloys Compd.*, 2009, **476**, 282–287.
19 I. A. Yakovlev, I. A. Tarasov and S. A. Lyashchenko, *J. Magn. Magn. Mater.*, 2017, **440**, 161–163.
20 B. Aronsson, D. H. Templeton, S. Rundqvist, E. Varde and G. Westin, *Acta Chem. Scand.*, 1960, **14**, 1414–1418.
21 S. Liang, R. Islam, D. J. Smith and P. A. Bennett, *J. Cryst. Growth*, 2006, **295**, 166–171.
22 M. A. Visotin, I. A. Tarasov, A. S. Fedorov, S. N. Varnakov and S. G. Ovchinnikov, *Acta Crystallogr., Sect. B: Struct. Sci.*, 2020, **76**, DOI: 10.1107/S2052520620005727.
23 X. Sun, X. Liu, X. Liu, Y. Meng, C. Song, Y. Yang, Y.-W. Li and X.-D. Wen, *J. Phys. Chem. C*, 2019, **123**, 11939–11949.
24 I. A. Tarasov, I. A. Yakovlev, M. S. Molokeev, M. Rautskii, I. V. Nemtsev, S. N. Varnakov and S. G. Ovchinnikov, *Mater. Lett.*, 2016, **168**, 90–94.
25 B.-X. Xu, Y. Zhang, H.-S. Zhu, D.-Z. Shen and J.-L. Wu, *Mater. Lett.*, 2005, **59**, 833–837.
26 C.-J. Chiou, S.-P. Chiu, J.-J. Lin and Y.-C. Chou, *CrystEngComm*, 2015, **17**, 4276–4280.
27 I. A. Tarasov, M. V. Rautskii, I. A. Yakovlev and M. N. Volochaev, *Semiconductors*, 2018, **52**, 654–659.
28 C. L. Hsin and Y. S. Tsai, *CrystEngComm*, 2016, **18**, 8155–8158.
29 W. Miiller, J. M. Tomczak, J. W. Simonson, G. Smith, G. Kotliar and M. C. Aronson, *J. Phys.: Condens. Matter*, 2015, **27**, 175601.
30 J. K. Tripathi, R. Levy, Y. Camus, M. Dascalu, F. Cesura, R. Chalasani, A. Kohn, G. Markovich and I. Goldfarb, *Appl. Surf. Sci.*, 2017, **391**, 24–32.
31 V. S. Zhandun, N. G. Zamkova, S. G. Ovchinnikov and I. S. Sandalov, *Phys. Rev. B*, 2017, **95**, 054429.
32 G. Cao, D. J. Singh, X.-G. Zhang, G. Samolyuk, L. Qiao, C. Parish, K. Jin, Y. Zhang, H. Guo, S. Tang, W. Wang, J. Yi, C. Cantoni, W. Siemons, E. A. Payzant, M. Biegalski, T. Z. Ward, D. Mandrus, G. M. Stocks and Z. Gai, *Phys. Rev. Lett.*, 2015, **114**, 147202.
33 Z.-Q. Zou, X. Li, X.-Y. Liu, K.-J. Shi and X.-Q. Guo, *Appl. Surf. Sci.*, 2017, **399**, 200–204.
34 D. Das, J. C. Mahato, B. Bisi, B. Satpati and B. N. Dev, *Appl. Phys. Lett.*, 2014, **105**, 191606.
35 J. Karel, J. Juraszek, J. Minar, C. Bordel, K. H. Stone, Y. N. Zhang, J. Hu, R. Q. Wu, H. Ebert, J. B. Kortright and F. Hellman, *Phys. Rev. B: Condens. Matter Mater. Phys.*, 2015, **91**, 144402.
36 I. A. Tarasov, M. A. Visotin, A. S. Aleksandrovsky, N. N. Kosyrev, I. A. Yakovlev, M. S. Molokeev, A. V. Lukyanenko, A. S. Krylov, A. S. Fedorov, S. N. Varnakov and S. G. Ovchinnikov, *J. Magn. Magn. Mater.*, 2017, **440**, 144–152.
37 M. N. Volochaev, I. A. Tarasov, Y. Y. Loginov, A. G. Cherkov and I. V. Kovalev, *J. Phys.: Conf. Ser.*, 2017, **857**, 012053.
38 I. A. Yakovlev, S. N. Varnakov, B. A. Belyaev, S. M. Zharkov, M. S. Molokeev, I. A. Tarasov and S. G. Ovchinnikov, *JETP Lett.*, 2014, **99**, 527–530.
39 T. Furuhara, T. Maki and K. Oishi, *Metall. Mater. Trans. A*, 2002, **33**, 2327–2335.
40 A. R. S. Gautam and J. M. Howe, *Philos. Mag.*, 2011, **91**, 3203–3227.
41 X. Wang, H. Huang, X. Gu, Y. Li, Z. Jia and Q. Liu, *J. Appl. Crystallogr.*, 2016, **49**, 1223–1230.
42 Q. Liang and W. T. Reynolds, *Metall. Mater. Trans. A*, 1998, **29**, 2059–2072.
43 X. F. Gu, T. Furuhara and W. Z. Zhang, *J. Appl. Crystallogr.*, 2016, **49**, 1099–1106.
44 V. G. Dubrovskii, N. V. Sibirev, G. E. Cirlin, M. Tchernycheva, J. C. Harmand and V. M. Ustinov, *Phys. Rev. E: Stat., Nonlinear, Soft Matter Phys.*, 2008, **77**, 031606.
45 L. A. Solovyov, *J. Appl. Crystallogr.*, 2004, **37**, 743–749.
46 V. Zhandun, N. Zamkova, S. Ovchinnikov and I. Sandalov, *JETP Lett.*, 2017, **106**, 582–586.
47 J. Kalt, M. Sternik, B. Krause, I. Sergueev, M. Mikolasek, D. Bessas, O. Sikora, T. Vitova, J. Göttlicher, R. Steininger, P. T. Jochym, A. Ptok, O. Leupold, H.-C. Wille, A. I. Chumakov, P. Piekarz, K. Parlinski, T. Baumbach and S. Stankov, *Phys. Rev. B*, 2020, **101**, 1–12.
48 I. Berbezier, J. Chevrier and J. Derrien, *Surf. Sci.*, 1994, **315**, 27–39.
49 B. Aronsson, D. H. Templeton, S. Rundqvist, E. Varde and G. Westin, *Acta Chem. Scand.*, 1960, **14**, 1414–1418.
50 L. Jelver, P. M. Larsen, D. Stradi, K. Stokbro and K. W. Jacobsen, *Phys. Rev. B*, 2017, **96**, 085306.
51 Y. Takagaki, J. Herfort, M. Ramsteiner, U. Jahn and B. Jenichen, *CrystEngComm*, 2018, **20**, 4173–4178.
52 Y.-T. Chiang, Y. Chou, C.-H. Huang, W.-T. Lin and Y.-C. Chou, *CrystEngComm*, 2019, **21**, 4298–4304.